Biosensors and Bioelectronics 55 (2014) 141–148

Contents lists available at ScienceDirect

Biosensors and Bioelectronics

journal homepage: www.elsevier.com/locate/bios

Effects of nanoparticle size and cell type on high sensitivity cell detection using a localized surface plasmon resonance biosensor

Fei Liu [a,b,e,1], Matthew Man-Kin Wong [c,b,1], Sung-Kay Chiu [c,b], Hao Lin [d,b], Johnny C. Ho [d,b], Stella W. Pang [a,b,*]

[a] Department of Electronic Engineering, City University of Hong Kong, Kowloon, Hong Kong
[b] Center for Biosystems, Neuroscience, and Nanotechnology, City University of Hong Kong, Kowloon, Hong Kong
[c] Department of Biology and Chemistry, City University of Hong Kong, Kowloon, Hong Kong
[d] Department of Physics and Materials Science, City University of Hong Kong, Kowloon, Hong Kong
[e] Department of Electronic Information Engineering, Tianjin University, Tianjin 300072, China

ARTICLE INFO

Article history:
Received 20 September 2013
Received in revised form
28 November 2013
Accepted 29 November 2013
Available online 10 December 2013

Keywords:
Au nanoparticles
Localized surface plasmon resonance (LSPR)
Cell concentration detection
Resonance peak shift
Human-derived retinal pigment epithelial RPE-1 cell
Breast cancer MCF-7 cell

ABSTRACT

A localized surface plasmon resonance (LSPR) effect was used to distinguish cell concentration on ordered arrays of Au nanoparticles (NPs) on glass substrates. Human-derived retinal pigment epithelial RPE-1 cells with flatter bodies and higher confluency were compared with breast cancer MCF-7 cells. Nanosphere lithography was used to form Au NPs with average diameters of 500 and 60 nm in order to compare cell detection range, resonance peak shift, and cell concentration sensitivity. A larger cell concentration range was detected on the larger 500 nm Au NPs compared to 60 nm Au NPs (8.56×10^3–1.09×10^6 vs. 3.43×10^4–2.73×10^5 cells/ml). Resonance peak shift could distinguish RPE-1 from MCF-7 cells on both Au NPs. RPE-1 cells consistently displayed larger resonance peak shifts compared to MCF-7 cells until the detection became saturated at higher concentration. For both types of cells, higher concentration sensitivity in the range of $\sim 10^4$–10^6 cells/ml was observed on 500 nm compared to 60 nm Au NPs. Our results show that cells on Au NPs can be detected in a large range and at low concentration. Optimal cell sensing can be achieved by altering the dimensions of Au NPs according to different cell characteristics and concentrations.

1. Introduction

Localized surface plasmon resonance (LSPR) spectroscopy of metallic nanoparticles (NPs) is a widely studied technique for efficient biosensor applications. Incident light on NPs induces collective oscillation of electrons at specific resonance wavelengths, resulting in enhanced intensity of localized electromagnetic (EM) field. Fabrication techniques such as chemical synthesis (Joshi et al., 2012), electron beam lithography (EBL; Cinel et al., 2012), and nanosphere lithography (NSL; Huang et al., 2012) have been adopted for NP preparation. The NSL method can provide a uniform template for fabricating long-range ordered NP arrays with low cost and high throughput, while the size and shape of the NPs can be adjusted in a controllable way (Jung and Byun, 2011).

The LSPR of Au NPs provides high sensitivity to short-range refractive index change (Δn, in refractive index unit (RIU)), and can be used for adsorbate concentration detection. The analyte concentration can be distinguished by corresponding resonance wavelength shifts ($\Delta\lambda_R$, in nm), which depend on the material, size, shape, and distribution of NPs. Refractive index sensitivity (RIS) is defined as $\Delta\lambda_R/\Delta n$; therefore high RIS is preferable for measuring low cell concentration. The commercial LightPath™ S4 system applies the LSPR principle, and uses the resonance peak shift of Au NPs to detect human IgG in the range of 0.1 μg/ml–5.0 mg/ml (LamdaGen, 2012). Higher detection sensitivity has also been demonstrated, with detection limits up to 0.1 ng/ml for thrombin and 1.6 nM for anti-human IgG (Cao et al., 2013; Guo and Kim, 2012). In addition, detection limits up to 8 pM have been demonstrated on 120 nm diameter Au NPs for extracellular adherence proteins found on the outer surface of the *Staphylococcus* (Chen et al., 2009). Nanoparticles have also been utilized to detect resonance peak shifts of *Escherichia coli* (*E. coli*) and *Salmonella*. For instance, 60 nm diameter Ag NPs (fabricated by EBL) could detect *E. coli* at a concentration of $\sim 10^7$ cfu/ml (Cinel et al., 2012), and synthesized Au nanorods with different aspect ratios could simultaneously detect *Salmonella* and *E. coli* at concentrations of 10^{12} cfu/ml (Wang and Irudayaraj, 2008). Using antibody-conjugated Au NPs to enhance intensity of localized EM fields,

* Corresponding author at: City University of Hong Kong, Department of Electronic Engineering, G6419, 83 Tat Chee Avenue, Kowloon, Hong Kong. Tel.: +852 344 298 53; fax: +852 3442 0562.
E-mail address: pang@cityu.edu.hk (S.W. Pang).
[1] These authors contributed equally to this work.

0956-5663/$ - see front matter © 2013 Elsevier B.V. All rights reserved.
http://dx.doi.org/10.1016/j.bios.2013.11.075

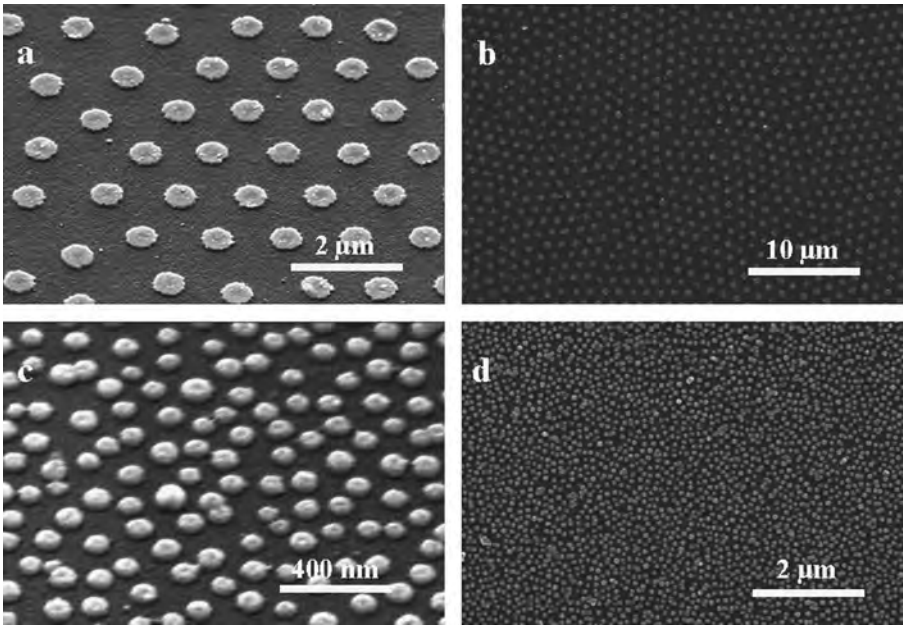

Fig. 1. Micrographs of fabricated Au nanoparticles (NPs) on glass substrates. (a, b) Diameter of Au NPs is ~500 nm. (c, d) Diameter of Au NPs is ~60 nm.

dark field optical microscopy can detect *E. coli* at concentrations of 2×10^4–6×10^4 cfu/ml (Xu et al., 2012). All these studies demonstrate cell detection methods that involve immobilizing corresponding antibodies on NPs. However, the concentration of *Salmonella* could not be distinguished by 30 nm diameter Au NPs. This limitation has been explained by the small contact area between the Au NPs and the rigid bodies of *Salmonella*, which leads to a small modification of the local electric field, and thus a plasmon peak shift that is always ~2–4 nm regardless of cell concentration (Fu et al., 2009). Therefore, it can be inferred that cell sensing performance depends on the dimensions of the NPs and the physical characteristics of the cell.

In addition to detecting biomolecules and bacteria, Au NPs have shown advantages for targeted diagnosis of cancer biomarkers and cancer cells (Perfézou et al., 2012), such as breast cancer cells (Lu et al., 2010) and oral epithelial cancer cells (EI-Sayed et al., 2005). Aptamers (nucleic acid ligand) conjugated Au NPs (Apt–Au NPs) can specifically bind with platelet-derived growth factor which is over-expressed in certain breast cancer cells. Thus the bound Apt–Au NPs in the breast cancer MDA-MB-231, Hs578T, and MCF-7 cells resulted in enhanced intensity of localized EM field, and this can be used to distinguish breast cancer cells from normal cells by dark field optical microscopy (Huang et al., 2009). In addition, electrochemical techniques based on Au NPs have been used for cell concentration detection (Costa et al., 2012; Arya et al., 2013); for instance the electrocatalytic method has been used for the quantification of human cancer HMy2 cells (Escosura-Muñiz et al., 2009). MCF-7 cancer cells can be detected in the range of 10^4–10^7 cells/ml by the electrochemical method (Li et al., 2010).

Here, we use the LSPR effect to distinguish the cell concentration of MCF-7 cancer cells on ordered arrays of Au NPs. The NSL method was used to form Au NPs on glass substrates with average diameters of 500 and 60 nm to compare cell detection range, resonance peak shift, and cell concentration sensitivity. Human-derived retinal pigmented epithelium RPE-1 cells that are flatter and exhibit contact inhibition were used for comparison with the smaller individual MCF-7 cells. Optimal cell sensing can be achieved by altering the dimensions of Au NPs according to different cell characteristics and concentrations. While small size (60 nm) NPs have been widely used for LSPR-based sensing of small size biomolecules, larger size NPs (500 nm) could be better in detecting larger size cells due to the longer EM field decay length and enhanced near-field electric field intensity due to the coupling between LSPR of NPs and the diffracted wave of the periodic NP arrays. Using this LSPR sensor for cell concentration measurement has advantages over traditional cell counting methods in that it can monitor changes in concentration of cells adhered on a solid surface in real time without any staining or cell removal from the surface as required by a hemocytometer. Time-lapse monitoring of the extinction spectra similar to the cell migration study could be utilized (Tang et al., 2013). In most applications, the use of a single cell type instead of multiple cell types is preferred as this can be used to figure out the direct effect of a drug or chemical on a single cell type such as liver cancer cell. Our results show that RPE-1 and MCF-7 cells can be detected in a large range and at low concentration based on the LSPR effect of Au NPs with defined diameters. To the best of our knowledge, this is the first study on applying the LSPR effect related to the shift of the resonance peak of NPs with various dimensions for detecting cell concentration without attachment of antibodies to NPs.

2. Experiment and methods

2.1. Fabrication of Au nanoparticles on glass substrates

The NSL method was used to form Au NPs on glass. A 2 nm thick Cr film and a 20 nm thick Au film were thermally evaporated on cleaned glass (8×12 mm^2). Polystyrene (PS) spheres were deposited as a mask, followed by Ar plasma etching to remove the uncovered Au and Cr films that were unprotected by the PS spheres. The remaining PS spheres were removed by O_2 plasma etching so as to leave the Au NPs on the glass, as shown in Fig. 1. For the fabrication of 500 nm Au NPs, PS spheres (10 wt%, 1270 nm diameter, microParticles GmbH, Berlin, Germany) were used and the Langmuir–Blodgett (LB) method was adopted to drive the PS spheres into a hexagonally arranged, close-packed monolayer (Zheng et al., 2008). Subsequently, an O_2 plasma with 20 sccm O_2, 50 W rf power, and 70 mTorr was used to reduce the diameter of each PS sphere from 1270 to 500 nm. These 500 nm PS spheres were separated by 770 nm and were used as a mask for Ar plasma etching of Cr/Au. An Ar plasma with 20 sccm Ar, 100 W rf power,

and 70 mTorr pressure was used to remove the Cr/Au films. For the fabrication of 60 nm Au NPs, PS spheres (sulfate-modified latex, 8% w/v 60 nm diameter, Life Technologies Limited, NY, USA) were deposited uniformly by electrostatic self-assembly on Au film treated with 5% w/v aluminum chlorohydrate (Adamas, CA, USA) as a monolayer etch mask (Andersson et al., 2007). O_2 plasma was not used to reduce NP size, but the rest of the fabrication process for forming the Au NPs using 60 nm diameter PS spheres was similar as described above.

2.2. Refractive index sensitivity tests

Extinction spectra with wavelengths ranging from 400 to 3200 nm were collected from Au NP coated glass substrates with an area of 12.6 mm^2. A spectrophotometer (PE Lambda 19, PerkinElmer, MA, USA) was used for the optical measurements. Light generated by a tungsten–halogen lamp was illuminated perpendicularly to the glass substrate, and the intensity of transmitted light was measured by a photomultiplier tube for visible light and a lead-sulfide cell for near infrared light. The extinction in % was calculated by subtracting the measured % transmission from 100.

The RIS of the 500 nm Au NPs was measured by submerging the glass substrates in the following media (with n being different refractive indices): air ($n=1.00$), n-hexane ($n=1.37$), and toluene ($n=1.50$). The RIS of 60 nm Au NPs was measured by submerging the glass substrates in the following media: air ($n=1.00$), water ($n=1.33$), acetone ($n=1.36$), and 2-propanol ($n=1.38$). Different media had to be used because water, acetone, and 2-propanol all have strong light absorption in the range of ~1300–3200 nm, and therefore cannot be used for 500 nm Au NPs (with major resonance peak occurring at 1900 nm).

2.3. Biosensing protocol

2.3.1. Sterilization of Au nanoparticles and cell culture preparation

Au NPs on glass substrates were rinsed with Milli-Q water, sterilized with 70% ethanol for 10 min, and air-dried in tissue culture hood before putting into 35 mm sterile tissue culture dishes.

RPE-1 and MCF-7 cells (American type culture collection, MD, USA) were routinely maintained in Dulbecco's modified eagle medium (DMEM) supplemented with 10% fetal bovine serum (FBS; Invitrogen, CA, USA), in a humidified incubator at 37 °C and 5% CO_2. Cell suspensions of 120 μl at different concentrations in DMEM and 10% FBS were loaded onto the surface of glass substrates with Au NPs, incubated at 37 °C for 2 h for cell attachment. Subsequently, 2 ml of DMEM with 10% FBS was added and the cells were incubated at 37 °C for 12 h before chemical fixation.

2.3.2. Cell fixing and extinction measurements

The cells on the surface of the glass substrates with Au NPs were rinsed twice with phosphate buffered saline (PBS; Invitrogen, CA, USA) and were fixed with freshly prepared 3% formaldehyde (Sigma, MO, USA) in PBS for 10 min at room temperature. Extinction spectrum measurements were conducted after the cells were air-dried on the 8 × 12 mm^2 glass substrate surface with Au NPs. The reference spectrum for extinction spectra without cells was collected using a sample consisted of a glass substrate without Au NPs, while the reference spectra for extinction spectra with cells at different concentrations were measured using samples consisted of glass substrates with the same corresponding cell concentrations but without Au NPs.

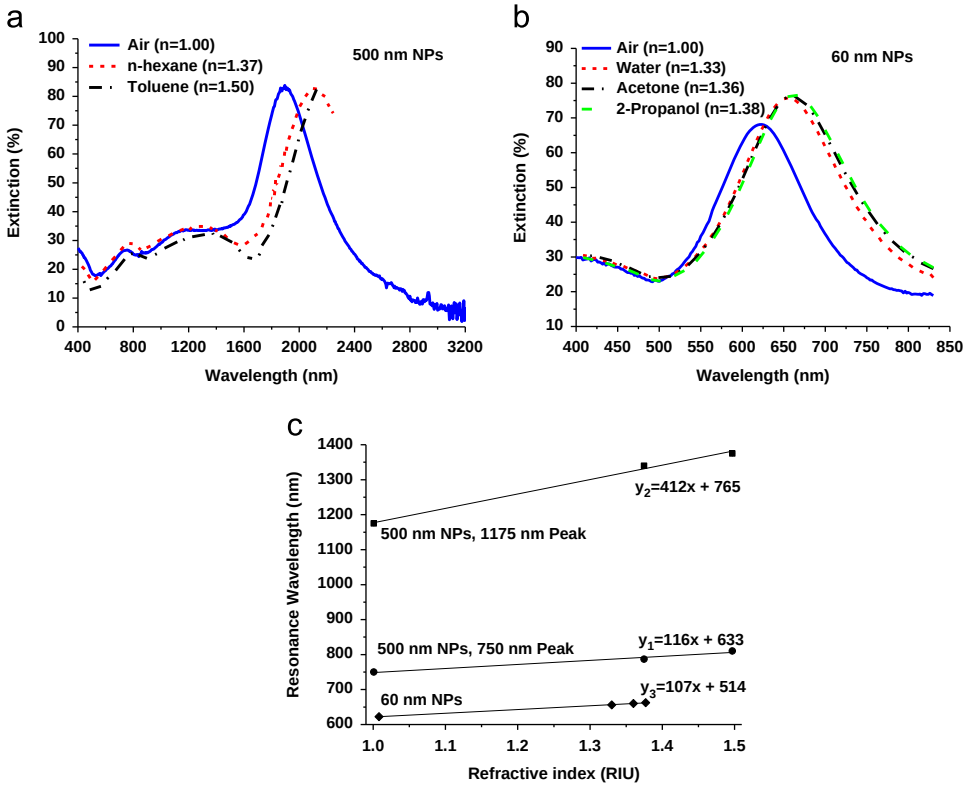

Fig. 2. (a) Extinction spectra of 500 nm Au NPs in different media: air with $n=1.00$, n-hexane with $n=1.37$, and toluene with $n=1.50$. (b) Extinction spectra of 60 nm Au NPs in different media: air with $n=1.00$, water with $n=1.33$, acetone with $n=1.36$, and 2-propanol with $n=1.38$. (c) Linear relationship between the LSPR wavelength and the refractive index of the 1175 and 750 nm resonance peaks of 500 nm Au NPs and 622 nm resonance peak of 60 nm Au NPs.

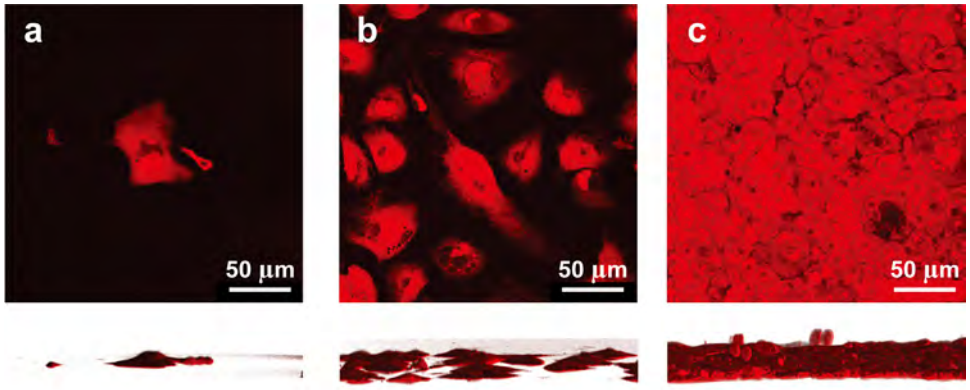

RPE-1	8.56×10^3 cells/ml	1.37×10^5 cells/ml	1.09×10^6 cells/ml
Surface area (μm^2)	3951	2449	609
% confluency	4.8	40.0	100.0
Thickness (μm)	8.7	9.0	17.7

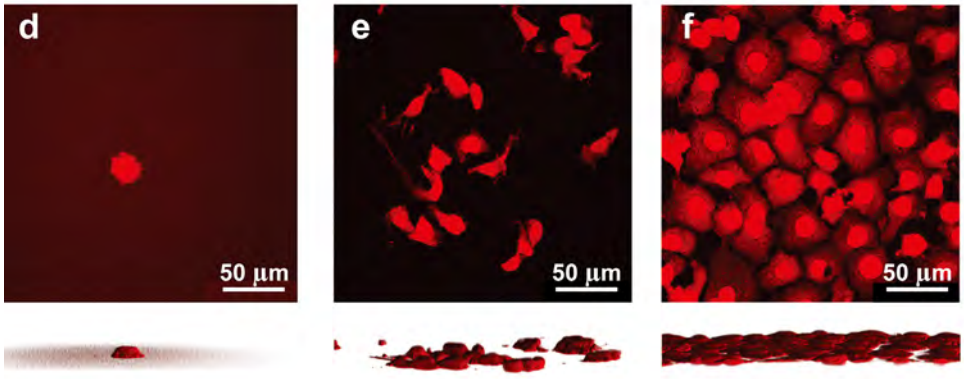

MCF-7	8.56×10^3 cells/ml	1.37×10^5 cells/ml	1.09×10^6 cells/ml
Surface area (μm^2)	682	545	928
% confluency	0.8	3.3	81.9
Thickness (μm)	10.1	8.8	7.1

Fig. 3. Maximum projections of 30 fluorescent confocal micrographs of the *X–Y* plane of RPE-1 (a)–(c) and MCF-7 (d)–(f) cells at different confluencies seeded on 60 nm Au NP coated glass substrates. RPE-1 cells with (a) 8.56×10^3 cells/ml, (b) 1.37×10^5 cells/ml, and (c) 1.09×10^6 cells/ml. MCF-7 cells with (d) 8.56×10^3 cells/ml, (e) 1.37×10^5 cells/ml, and (f) 1.09×10^6 cells/ml. The figure below each micrograph is the Z-stack of micrographs to show the thickness of the cell layer. Information on cell surface area, percentage confluency, and maximum cell thickness of RPE-1 and MCF-7 cells at different concentrations are summarized below each set of micrographs.

2.4. Scanning electron and confocal microscopy measurements

Au NPs on glass substrates were observed under an environmental scanning electron microscope (XL30 ESEM-FEG, Philips Electronics, Netherlands), after coating with Au–Pd using a sputter-deposition coater (SCD005, Leica Microsystems, Wetzlar, Germany). To measure the surface area and thickness of the cells on the glass surface, the cells were fixed with 3% formaldehyde in PBS for 10 min, permeabilized in 0.2% Triton X-100 (Sigma, MO, USA) in PBS for 10 min, and stained with 2 μg/ml propidium iodide (Sigma, MO, USA) for 20 min at room temperature. The cells were mounted on 24×50 mm^2 cover glasses of thickness no. 1 (Marienfeld-SupeRior, Lauda-Königshofen, Germany) using a Vectashield mounting medium (Vector Laboratories, CA, USA). Fluorescence signals from the cells were photographed using a confocal laser microscope (TCS-SPE, Leica Microsystems, Wetzlar, Germany) and the cells were scanned using a step size of 250 nm. The micrographs from all scanned layers were compiled, and the maximum projections of these images were generated by ImageJ version 1.47v (NIH, MD, USA) to compute the surface area. Using the Volume Viewer plugin, the average distances from the bottom of the cells to the peak (thicknesses; $n=10$) were measured on the cells of different concentrations.

3. Results and discussion

3.1. High refractive index sensitivity of Au nanoparticles

Extinction spectra of both 500 and 60 nm Au NPs are measured in media with different refractive indices as shown in Fig. 2(a) and (b). The ratio of the surface area occupied by the 500 and 60 nm Au NPs was 15.5% and 27.7%, respectively. The measured extinction is close to the simulated results for the 60 nm Au NPs and the enhanced near-field electric field intensity effect related to the coupling between the LSPR of NP and the diffracted wave of the periodic 500 nm NP array (Chu et al., 2008). The dipole plasmon resonance peak was at 1900 nm for the 500 nm Au NPs measured in air ($n=1.00$), and it blue-shifted to 622 nm when the diameter of the Au NPs was reduced to 60 nm. Also, the corresponding full width at half maximum (FWHM) was narrowed from

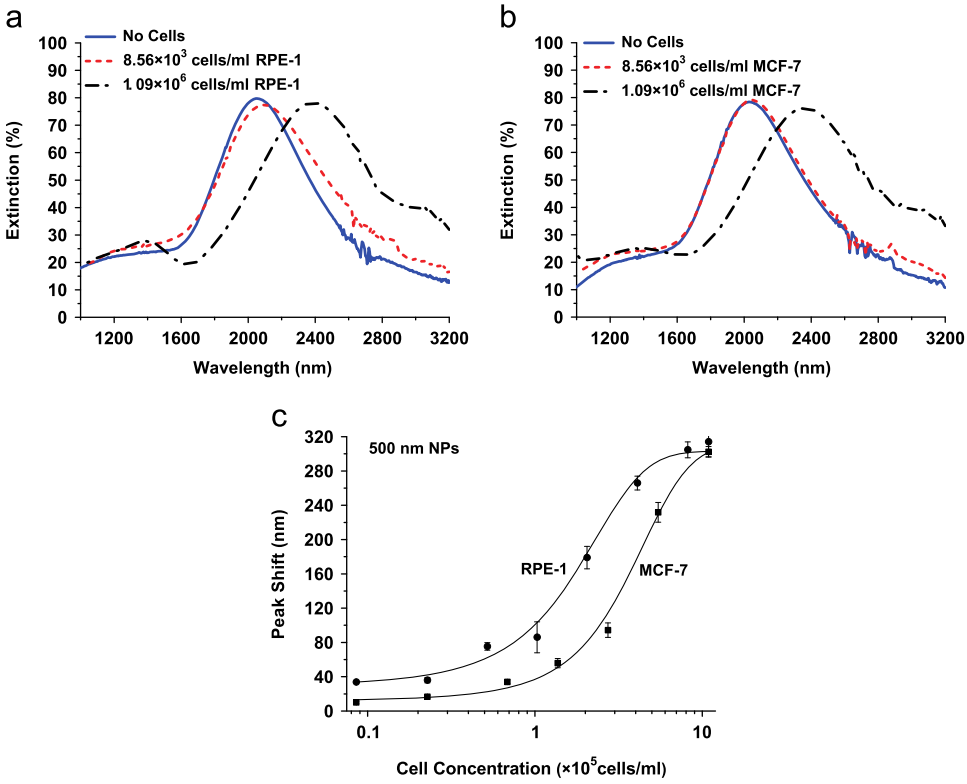

Fig. 4. (a, b) Extinction spectra of 500 nm Au NPs without cells and with cells of concentration 8.56×10^3 and 1.09×10^6 cells/ml. (a) RPE-1 cells and (b) MCF-7 cells. (c) For 500 nm Au NPs, LSPR peak shift as a function of RPE-1 and MCF-7 cell concentration in the range 8.56×10^3–1.09×10^6 cells/ml.

400 to 120 nm. For 500 nm Au NPs, two weak resonance peaks at shorter wavelengths of 750 and 1175 nm were also present, which has been explained by the different plasmon modes related to non-uniform fabrication (Cai et al., 2012; Ding et al., 2011).

The RIS of Au NPs was measured by submerging the glass substrates in media with different refractive indices. The resonance peaks red-shifted linearly with increasing refractive index of surrounding medium, which is shown in Fig. 2. The measured RIS was 107 nm/RIU for the 60 nm Au NPs. For the 500 nm Au NPs, the RIS was 116 nm/RIU for the 750 nm resonance peak and 412 nm/RIU for the 1175 nm resonance peak. This shows that the RIS is higher when the resonance peak at longer wavelength is used for the same Au nanostructure, a phenomenon that has been previously observed (Larsson et al., 2007). Due to the limitation of the solutions' light absorption in the near infrared region, only the resonance peaks in air and n-hexane were obtained for the 1900 nm peak. However, this peak has much larger RIS, because when the refractive index was changed from 1.00 to 1.37 in different media, the corresponding 200 nm peak shift was almost 5 × larger than the 622 nm peak shift for 60 nm NPs. For 500 nm Au NPs, the 1900 nm dipole resonance peak had a larger extinction and RIS compared to 750 and 1175 nm resonance peaks, and was therefore adopted for cell sensing measurements.

3.2. RPE-1 and MCF-7 cells immobilized on Au nanoparticles

RPE-1 and MCF-7 cells were both tested to study the relationship between the LSPR shift and cell characteristics. The typical diameter of an individual RPE-1 cell (after trypsinization and resuspension in PBS) was measured to be ~20 μm by a Coulter counter, which was slightly larger than that of MCF-7 cells with diameter ~18 μm. The percentage of area covered by the cells on substrates, defined as % confluency, was higher for RPE-1 cells than that for MCF-7 cells at the same cell concentration. At low confluency (< 50%), the surface area covered by each RPE-1 cell (2449–3951 μm^2) was much larger than that of an MCF-7 cell (545–682 μm^2) when seeded onto the Au NP coated glass substrates (Fig. 3(a), (b), (d), and (e)). In contrast, when the cells were grown to confluence, the average cell surface area of MCF-7 cells was larger (928 μm^2) than that of RPE-1 cells (609 μm^2). This observation is likely due to the fact that the larger cell surface area of RPE-1 cells enabled full cell–cell contact (confluence) when 1.09×10^6 cells/ml cells were seeded onto the glass surface.

Typically, the center of mammalian cells contains the nucleus and is the thickest part with thickness gradually decreasing along the cell edges. Overall, cell–cell contact was not observed at low concentration as shown in Fig. 3(a), (b), (d), and (e). As cell concentration increased, cells formed a monolayer cover on the Au NP coated glass surfaces. At high concentration, cells were in close proximity with each other as shown in Fig. 3(c) and (f). At concentrations of 1.09×10^6 cells/ml, the larger RPE-1 cells completely covered the entire Au NP coated glass surface, and a few cells started to stack on top of the others as shown in Fig. 3(c). The maximum thickness of RPE-1 cells at high confluency was 17.7 μm, with some cells forming the second layer, while MCF-7 cells were only 7.1 μm thick with the same number of cells seeded on the surface (Fig. 3(c) and (f)). For RPE-1 cells, the thickness of the cell layers decreased with lower cell confluence, while the cell layer of MCF-7 increased in less crowded conditions. We found similar cell adsorption behavior and no statistical differences of both types of the adhered cells on arrays of Au NPs of different sizes and on bare glass substrates.

3.3. Dependence of resonance peak shift on confluency of cells on 500 nm Au nanoparticles

The extinction spectra of the 500 nm Au NPs with RPE-1 and MCF-7 cells at concentrations of 8.56×10^3 and 1.09×10^6 cells/ml were measured after the cells were fixed and air dried on the Au

NP coated glass substrates, as shown in Fig. 4(a) and (b). For both types of cells, there was a red-shift of the resonance wavelength after the cells were fixed (due to the increased refractive index caused by the cell layer on the Au NPs), and this shift increased with increasing cell concentration. The width of the resonance peak increased with the radiative and non-radiative damping (Wokaun et al., 1982; Zorić et al., 2011). The spectra were broadened with higher cell concentration on the Au NPs because both the radiative and non-radiative damping increased related to the larger refractive index at higher cell concentration (Maier, 2007; Mortazavi et al., 2012). The resonance peak shift ($\Delta\lambda_R$) in response to a change of refractive index due to the presence of cells on the Au NP coated glass surface can be described as (Jung et al., 1998) follows:

$$\Delta\lambda_R \approx m(n_{adsorbate} - n_{medium})(1 - e^{(-2d/l_d)}) \quad (1)$$

where m is the RIS of the Au NPs (nm/RIU), n_{medium} is the refractive index of the surrounding medium, $n_{adsorbate}$ is the refractive index of the adsorbate in a form of uniform film with thickness d (in nm), and l_d (in nm) is the EM field decay length of the Au NPs.

Mammalian cells contain numerous organelles with different refractive indices. Therefore the protein concentration within the cells mainly determines the effective refractive index of the cells because of its higher refractive index of 1.50–1.58. Cells with more proteins such as cancer cells have a relatively larger refractive index. The refractive index of immobilized MCF-7 cancer cells ranges from 1.39 to 1.40, which is slightly larger than the typical value of 1.35–1.37 for a normal cell (Liang et al., 2007). Since the immobilized cells form the adsorbate islands or closely packed layers on the Au NP surface, the effective thickness d of the cell layer should be properly weighted by the surface area, confluency, actual thickness, and concentration of the cells. The EM field decays exponentially with the decay length l_d, which depends on the size and shape of the Au NPs. Previous studies have shown that EM field decay length l_d is ~52 nm for Au NPs with 70 nm widths (Haes et al., 2004). Au crescent nanostructures with 410 nm diameter show a 692 nm EM field decay length for the ~2300 nm long-axis dipole resonance peak (Bukasov et al., 2010). The EM field decay length increases with the size of Au NPs (Kedem et al., 2011). This gives us a general idea of the decay lengths of the 500 and 60 nm Au NPs used in our work.

Fig. 4(c) shows the resonance peak shifts of the 500 nm Au NPs for the cell concentrations within a range of 8.56×10^3–1.09×10^6 cells/ml. All the results on resonance peak shifts were obtained from at least three sets of separately prepared sensors at each cell concentration. To demonstrate reproducibility, an additional three sets of sensors at all seven different cell concentrations were measured for the MCF-7 cells, providing a total of six different sets of samples shown in Fig. 4(c) for the MCF-7 cells. As expected, the resonance peak shift and sensing efficiency greatly depend on the surface area, confluency, thickness, and concentration of the cells. At each concentration, RPE-1 cells covered a higher confluency on the surface with Au NPs compared to MCF-7 cells, which resulted in a larger value of effective thickness d. Therefore, resonance peak shift of RPE-1 cells was larger than that of MCF-7 cells. With increasing cell concentration, the separation between two cells became smaller, and the cells were closely packed and reached confluence at the concentration of 1.09×10^6 cells/ml for RPE-1 cells, as shown in Fig. 3(c). The thickness d increases with cell concentration and becomes comparable with or even thicker than the EM field decay length l_d. Therefore, at higher concentration, the EM field of Au NPs is not sensitive to the increasing cell concentration, or the effective thickness d. Accordingly, APRE-19 cells at higher confluency became saturated at lower concentration compared with MCF-7 cells. The slopes of the linear fitting curves describe the cell sensing sensitivity (resonance peak shift/cell concentration, nm/(cells/ml)). Since the slope is 60 for RPE-1 cells and 38 for MCF-7 cells for concentrations below 4.1×10^5 cells/ml, this indicates that the 500 nm Au NPs are more sensitive to the change in concentration of RPE-1 cells in this range. This is due to the larger surface area of RPE-1 cells which causes a more rapid increase of cell confluency and thickness, and hence corresponding effective thickness d. By taking difference of peak shift between two cell concentrations and standard error of mean (SEM) for three to six sets of sensors into account, the detection ranges for RPE-1 and MCF-7 cells are 2.28×10^4–8.20×10^5 and 8.56×10^3–1.09×10^6 cells/ml, respectively.

We have analyzed the SEM among each three sets of data. Within the detection limits, the SEM at a given concentration is always smaller than the difference in resonance peak shift when the cell concentration is changed. In addition, we further tested the reproducibility using three additional sets of 500 nm Au NP sensors (total of six sets) for MCF-7 cells as shown in Fig. 4(c). Again, the results are reproducible among six sets of separately prepared sensors at various concentrations with SEMs smaller than the differences of resonance peak shifts. For example, for MCF-7 cells at the lowest two concentrations, the difference of average resonance peak shift is 6.7 nm while the SEM is only 1.5 nm. Therefore, we can conclude that the results from multiple sets of sensors at various concentrations, as well as the dependence of the resonance peak shift on cell concentration, are reproducible.

3.4. Dependence of resonance peak shift on confluency of cells on 60 nm Au nanoparticles

60 nm Au NPs were also studied for RPE-1 and MCF-7 cell concentration detection. For 60 nm Au NPs, the RIS is only 107 nm/RIU, which is much smaller than the 535 nm/RIU measured for 500 nm Au NPs. On the other hand, since the resonance peak is in the visible light region, the 60 nm Au NPs have the advantage of being able to detect living cells in solution without light absorption by the aqueous solution.

The extinction spectra of 60 nm Au NPs with RPE-1 and MCF-7 cells at concentrations of 8.56×10^3 and 5.45×10^5 cells/ml are shown in Fig. 5(a) and (b). For 60 nm Au NPs, the resonance wavelength was ~622 nm (vs. ~1900 nm for 500 nm Au NPs), and also the extinction increased with increasing cell concentration for both cell types (unlike 500 nm Au NPs, as shown in Fig. 4(a) and (b)). A probable explanation for this difference is that the extinction is affected by both the refractive index of the surrounding adsorbate and medium ($n_{(adsorbate+medium)}$), and the radiative damping and non-radiative damping, and is approximately inversely proportional to the imaginary part of the Au dielectric constant (ε_2) (Moores and Goettmann, 2006; Mortazavi et al., 2012; Zhang et al., 2011). For resonance peaks around 622 nm, the change of ε_2 due to the red-shifted peak at higher cell concentration is much smaller than that of resonance peaks around 1900 nm (Palik, 1985). Therefore, for 60 nm Au NPs, larger extinction was obtained for cells at higher concentration, compared to the 500 nm Au NPs.

Fig. 5(c) shows the resonance wavelength peak shifts of the 60 nm Au NPs for cell concentrations within a range of 8.56×10^3–5.45×10^5 cells/ml. The relationship between cell concentration and resonance peak shift shows similar trends compared to 500 nm Au NPs, as shown in Fig. 4(c). For instance, RPE-1 cells at higher confluency became saturated at lower concentration (1.37×10^5 cells/ml) compared with MCF-7 cells. On the other hand, MCF-7 cells began to show a larger peak shift compared to RPE-1 cells for cell concentration above 2.73×10^5 cells/ml, which

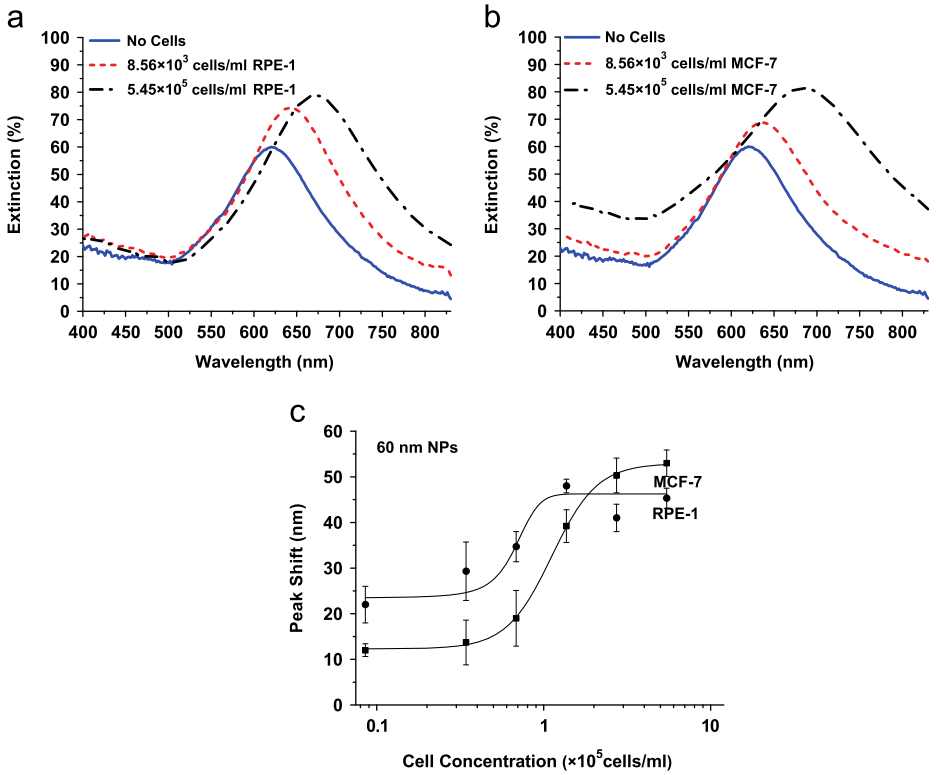

Fig. 5. (a, b) Extinction spectra of 60 nm Au NPs without cells and with cells of concentration 8.56×10^3 and 5.45×10^5 cells/ml. (a) RPE-1 cells and (b) MCF-7 cells. (c) For 60 nm Au NPs, LSPR peak shift as a function of RPE-1 and MCF-7 cell concentration in the range 8.56×10^3–5.45×10^5 cells/ml.

could imply that MCF-7 cells have a larger refractive index since the resonance peak shift depends mainly on the refractive index of the cells at high concentrations.

Since the slope of the linear fitting curves is 20 for RPE-1 cells and 22 for MCF-7 cells for concentrations between 3.43×10^4 and 1.37×10^5 cells/ml, this indicates that 60 nm Au NPs have a similar sensitivity for both cell types in this range of cell concentration. The similarity in sensitivity is mainly due to the local EM field with short decay length l_d (in the order of tens of nm) for small size NPs (Haes et al., 2004), which is much smaller compared to the effective thickness d (in the order of a few μm). Therefore, the cell concentration detection sensitivity for 60 nm Au NPs will be similar for different cell types due to the exponential dependence of d/l_d in Eq. (1) when l_d is much smaller than d. Overall, by taking difference of peak shift and SEM into account, the detection ranges for RPE-1 and MCF-7 cells are 3.43×10^4–1.37×10^5 and 3.43×10^4–2.73×10^5 cells/ml, respectively, for 60 nm sensors.

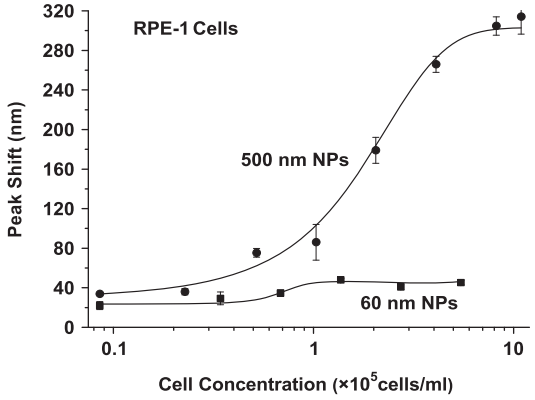

Fig. 6. Comparison of RPE-1 cell concentration detections using 500 and 60 nm Au NPs.

3.5. Cell sensing comparison of 500 and 60 nm Au nanoparticles

500 nm Au NPs show a much larger RIS and a longer EM field decay length compared to 60 nm Au NPs. The sensing performance of 500 and 60 nm Au NPs for RPE-1 cells is compared in Fig. 6. Due to the larger RIS, the saturated resonance peak shift of 500 nm Au NPs is almost 6× larger than that of 60 nm Au NPs (~300 vs. ~50 nm). A similar peak shift ratio was also obtained with the extinction spectra of Au NPs measured in media with different refractive indices, as shown in Fig. 2. Due to the longer EM field decay length l_d for 500 nm Au NPs, a larger cell concentration range was detected on 500 nm compared to 60 nm Au NPs (8.56×10^3–1.09×10^6 vs. 3.43×10^4–2.73×10^5 cells/ml).

Optimal cell sensing can be achieved by altering the dimensions of Au NPs according to different cell characteristics and concentrations. For the detection of the flatter MCF-7 cells, 500 nm Au NPs show more efficient sensing than 60 nm Au NPs in the concentration range of 8.56×10^3–1.09×10^6 cells/ml. Therefore, 500 nm Au NPs should be used for optimal cell sensing of larger cells at higher concentrations. On the other hand, with resonance peaks in the visible light region, the 60 nm Au NPs are preferable for the detection of living cells in aqueous solution. Using the 60 nm Au NPs, we can measure dynamic, live cell concentration using time-lapse monitoring of extinction spectra such as: (1) detecting decrease in the number of cells present on the sensors with time when the adhered cancer cells are subjected to cancer therapeutic drugs that can induce apoptosis and (2) measuring the dynamic increase in cell concentration across the NP array platform placed next to a confluent monolayer of epithelial cells and measure the rate of migration onto the array—an assay for cancer cell metastasis or wound healing. Chemical reagents can also be used with this sensor for screening therapeutics in inhibiting metastasis and wound healing.

4. Conclusions

The LSPR effect has been used to distinguish RPE-1 and MCF-7 cell concentration on ordered arrays of Au NPs on glass substrates formed by the NSL method. Sensing efficiency depended on the size, shape, and distribution of the Au NPs as well as the confluency and concentration of RPE-1 and MCF-7 cells. Larger size (500 nm) NPs have longer EM field decay length, and they provide a larger detection range than that of smaller size (60 nm) NPs. For MCF-7 cells, the detection range for 500 nm NPs is 8.56×10^3–1.09×10^6 cells/ml compared to 3.43×10^4–2.73×10^5 cells/ml for 60 nm NPs. On the other hand, flatter cells that spread out on a larger area (RPE-1) displayed larger resonance peak shifts than those of small size cells (MCF-7). These characteristics can be used to distinguish RPE-1 from MCF-7 cells. Our results show that cells on LPSR-based sensor that consisted of Au NPs can be detected in a large range and at low concentration. Therefore, optimal cell sensing can be achieved by altering the dimensions of Au NPs according to different cell characteristics and concentrations.

Acknowledgments

This work was supported by the Center for Biosystems, Neuroscience, and Nanotechnology of City University of Hong Kong under Project number 9360148. We gratefully acknowledge Dr. Qing Yuan Tang, Miss Tsing Chung, Dr. Polis Wong, Mr. Robust Lai, Dr. Payton Lin, Dr. Shang Xin Lin, Mr. Bing Zou, and Mr. Michael Chiang for their technical support and helpful discussions.

References

Andersson, A-S., Glasmästar, K., Hanarp, P., Seantier, B., Sutherland, D.S., 2007. Nanotechnology 18, 205303.
Arya, S.K., Wang, Y.P., Wong, C.C., Rahman, A.R.A., 2013. Biosens. Bioelectron. 41, 446–451.
Bukasov, R., Ali, T.A., Nordlander, P., Shumaker-Parry, J.S., 2010. ACS Nano 4 (11), 6639–6650.
Cai, Y.J., Li, Y., Nordlander, P., Cremer, P.S., 2012. Nano Lett. 12, 4881–4888.
Cao, J., Tu, M.H., Sun, T., Grattan, K.T.V., 2013. Sens. Actuators B 181, 611–619.
Chen, S., Svedendahl, M., Käll, M., Gunnarsson, L., Dmitriev, A., 2009. Nanotechnology 20, 434015.
Chu, Y.Z., Schonbrun, E., Yang, T., Crozier, K.B., 2008. Appl. Phys. Lett. 93, 181108.
Cinel, N.A., Bütün, S., Özbay, E., 2012. Opt. Express 20 (3), 2587–2597.
Costa, M.M.D., Escosura-Muñiz, A.D.L., Nogués, C., Barrios, L, Ibáñez, E., Merkoçi, A.A., 2012. Small 8 (23), 3605–3612.
Ding, P., Liang, E.J., Hu, W.Q., Cai, G.W., Xue, Q.Z., 2011. Photon. Nanostruct. 9, 42–48.
EI-Sayed, I.H., Huang, X.H., EI-Sayed, M.A., 2005. Nano Lett. 5 (5), 829–834.
Escosura-Muñiz, A.D.L., Sánchez-Espinel, C., Díaz-Freitas, B., González-Fernández, Á., Costa, M.M., Merkoçi, A., 2009. Anal. Chem. 81, 10268–10274.
Fu, J.X., Park, B., Zhao, Y.P., 2009. Sens. Actuators B 141, 276–283.
Guo, L.H., Kim, D.H., 2012. Biosens. Bioelectron. 31, 567–570.
Haes, A.J., Zou, S.L., Schatz, G.C., Van Duyne, R.P., 2004. J. Phys. Chem. B 108, 109–116.
Huang, C.J., Ye, J., Wang, S., Stakenborg, T., Lagae, L., 2012. Appl. Phys. Lett. 100, 173114.
Huang, Y.F., Lin, Y.W., Lin, Z.H., Chang, H.T., 2009. J. Nanopart. Res. 11, 775–783.
Joshi, G.K., McClory, P.J., Dolai, S., Sardar, R., 2012. J. Mater. Chem. 22, 923–931.
Jung, L.S., Campbell, C.T., Chinowsky, T.M., Mar, M.N., Yee, S.S., 1998. Langmuir 14, 5636–5648.
Jung, W.K., Byun, K.M., 2011. Biomed. Eng. Lett. 1, 153–162.
Kedem, O., Tesler, A.B., Vaskevich, A., Rubinstein, I., 2011. ACS Nano 5 (2), 748–760.
LamdaGen, 2012. Available online: ⟨http://lamdagen.com/lspr-label-free-detection⟩.
Larsson, E.M., Alegret, J., Käll, M., Sutherland, D.S., 2007. Nano Lett. 7 (5), 1256–1263.
Li, T., Fan, Q., Liu, T., Zhu, X.L., Zhao, J., Li, G.X., 2010. Biosens. Bioelectron. 25, 2686–2689.
Liang, X.J., Liu, A.Q., Lim, C.S., Ayi, T.C., Yap, P.H., 2007. Sens. Actuators A 133, 349–354.
Lu, W.T., Arumugam, S.R., Senapati, D., Singh, A.K., Arbneshi, T., Khan, S.A., Yu, H.T., Ray, P.C., 2010. ACS Nano 4 (3), 1739–1749.
Maier, S.A., 2007. Plasmonics: Fundamentals and Applications. Springer Science+Business Media LLC, New York.
Moores, A., Goettmann, F., 2006. New J. Chem. 30, 1121–1132.
Mortazavi, D., Kouzani, A.Z., Kaynak, A., Duan, W., 2012. Prog. Electromagn. Res. 126, 203–235.
Palik, E.D., 1985. Handbook of Optical Constants of Solids. Academic Press, San Diego.
Perfézou, M., Turner, A., Merkoçi, A., 2012. Chem. Soc. Rev. 41, 2606–2622.
Tang Q.Y., Tong Y., Lam Y.W., Shi P., Pang, S.W., 2013. Proceeding of the International Conference on Electron, Ion, and Photon Beam Technology and Nanofabrication, Tennessee, USA.
Wang, C.G., Irudayaraj, J., 2008. Small 4 (12), 2204–2208.
Wokaun, A., Gordon, J.P., Liao, P.F., 1982. Phys. Rev. Lett. 48 (14), 957–960.
Xu, X., Chen, Y., Wei, H.J., Xia, B., Liu, F., Li, N., 2012. Anal. Chem. 84, 9721–9728.
Zhang, S.P., Bao, K., Halas, N.J., Xu, H.X., Nordlander, P., 2011. Nano Lett. 11, 1657–1663.
Zheng, Y.B., Juluri, B.K., Mao, X.L., Walker, T.R., Huang, T.J., 2008. J. Appl. Phys. 103, 014308.
Zorić, I., Zäch, M., Kasemo, B., Langhammer, C., 2011. ACS Nano 5 (4), 2535–2546.